Journal of Chromatography A, 1218 (2011) 46–56

Contents lists available at ScienceDirect

Journal of Chromatography A

journal homepage: www.elsevier.com/locate/chroma

Effective medium theory expressions for the effective diffusion in chromatographic beds filled with porous, non-porous and porous-shell particles and cylinders. Part II: Numerical verification and quantitative effect of solid core on expected B-term band broadening

Sander Deridder, Gert Desmet*

Vrije Universiteit Brussel, Department of Chemical Engineering, Pleinlaan 2, 1050 Brussels, Belgium

ARTICLE INFO

Article history:
Received 8 July 2010
Received in revised form 5 October 2010
Accepted 25 October 2010
Available online 30 October 2010

Keywords:
Numerical simulations
B-term
Longitudinal diffusion
Peak parking
Effective medium theory
Porous-shell particles

ABSTRACT

The results of a numerical simulation study of the diffusion and retention in fully porous spheres and cylinders are compared with some of the high order accuracy analytical solutions for the effective diffusion coefficient that have been derived from the effective medium theory (EMT) theory in part I of the present study. A variety of different ordered (spheres and cylinders) and disordered (cylinders) packings arrangements has been considered. The agreement between simulations and theory was always excellent, lying within the (very tight) accuracy limits of the simulations over the full range of retention factor and diffusion constant values that is practically relevant for most LC applications. Subsequently filling up the spheres and cylinders with a central solid core, while keeping the same packing geometry and the same mobile phase (same thermodynamic retention equilibrium), it was found that the core induces an additional obstruction which reduces the effective intra-particle diffusion coefficient exactly with a factor $\gamma_{part} = 2/(2+\rho^3)$ for spherical particles and $\gamma_{part} = 1/(1+\rho^2)$ for cylinders (ρ is the ratio of the core to the particle diameter, $\rho = d_{core}/d_{part}$). These expressions hold independently of the packing geometry, the value of the diffusion coefficients and the equilibrium constant or the size of the core. The expressions also imply that, if considering equal mobile phase conditions, the presence of the solid core will never reduce the particle contribution to the B-term band broadening with more than 33% (50% in case of cylindrical pillars).

1. Introduction

A proper understanding of he B-term band broadening, i.e., the single source of band broadening that remains when the flow is switched off, has become very important again with the recent re-introduction of porous-shell particles [1,2]. Despite the fact that most manufacturers of these columns market their columns with the argument of a reduced stationary zone mass transfer resistance (C_s-term band broadening), these columns owe their exceptionally low reduced plate heights to a significant extent also to a remarkably low B-term band broadening (next to a lower A-term and C-term band broadening) [3].

Given its physical meaning, the best way to measure the B-term band broadening is by measuring the band broadening at very low flow rates, or, even better, at zero flow rate. In the latter case, one generally uses the term "peak parking" method, a method first used by Knox [4,5] and invented during a famous taxi ride with Giddings [6]. Briefly, this method is based on measuring the difference in band variance between bands eluting from a column after having been arrested for different "parking times" Δt_{park} [5,7]. According to the Einstein–Schmoluchowski law, $\Delta\sigma^2$ and Δt_{park} can be expected to vary according to a perfect linear relationship:

$$\Delta\sigma^2 = 2 \cdot D_{eff} \cdot \Delta t_{park} \quad (1)$$

The proportionality factor ($2.D_{eff}$) is directly linked to the B-term plate height contribution via [5]:

$$h_B = \frac{B}{\nu_0} = 2.\frac{D_{eff}/D_m}{\nu_0} \cdot (1+k') = \frac{2 \cdot \gamma_{eff}}{\nu_0} \cdot (1+k') \quad (2)$$

In Eqs. (1) and (2), D_{eff} represents the effective diffusion coefficient experienced by the analytes while randomly diffusing through the interstitial space and the meso-porous zone of the particles.

To interpret the measurements of D_{eff} and the B-term constant in terms of the fundamental physicochemical and mass transport coefficients, a sound theoretical model is needed. During the

* Corresponding author. Tel.: +32 2 629 32 51; fax: +32 2 629 32 48.
E-mail address: gedesmet@vub.ac.be (G. Desmet).

0021-9673/$ – see front matter © 2010 Elsevier B.V. All rights reserved.
doi:10.1016/j.chroma.2010.10.086

Nomenclature

Symbols

a_1	a_2, coefficients in Eq. (14), values see Table 1 of part I
b_1	b_2, b_3, coefficients in Eq. (9b), values see Table 1 of part I
B	B-term constant, see Eq. (2)
c	concentration of tracer [mol/m^3]
d	diameter [m]
D	diffusion coefficient [m^2/s]
h_B	dimensionless B-term plate height contribution ($=H_B/d_{part}$)
k'	phase retention factor
k''	zone retention factor
K	equilibrium distribution constant
n	direction normal to the surface

Greek symbols

α	permeability ratio
β_1	β_2, β_3, see Eq. (9b)
$\Delta\sigma^2$	difference in spatial variance [m^2]
Δt_{park}	parking time [s]
ε	porosity
γ	obstruction factor
Λ	see Eq. (9b)
ν_0	reduced velocity of an unretained component ($=u_0 d_{part}/D_m$)
ρ	relative core diameter ($\rho = d_{core}/d_{part}$)
ζ_2	Torquato's three-point factor

Subscripts

A, pz	relating to analyte A in porous zone
core	core
e	external
eff	effective
FP	fully porous
m	molecular
part	particle-based
pz	porous zone-based
s	stationary phase
T	total

years, many types of modelling have been applied to the field of chromatography, ranging from analytical solutions to the fundamental mass conservation laws [1,2], microscopic and stochastical modelling [8–10], Lattice–Boltzmann simulations [11,12], computational fluid dynamics (CFD) [13–15].

In the present study, the latter approach has been used to verify the accuracy of the effective medium theory (EMT) expressions established in part I. This validation is needed because the EMT-expressions of Torquato [16] and Cheng and Torquato [17] that are presented there were originally established for electrical and thermal conductivity and have to the best of our knowledge never been transformed in terms of the permeability of a binary medium with a partitioning equilibrium between its two composing phases, as is encountered in chromatographic columns. In [15], we could already demonstrate that two other EMT-models (the Maxwell-model and the Landauer–Davis model) yielded a relatively good agreement with the B-term dispersion calculated using CFD in 2D arrays of cylindrical pillars. However, the agreement was not perfect. For the Landauer–Davis (LD) model, it is clear from part I that this was due to the fact that this model is simply not suited to represent the diffusion in particulate media, because it is based on a phase-symmetry assumption [18], implying that one should expect the same effective diffusion if the particles and the interstitial void would switch diffusion properties. Clearly this assumption is in conflict with the physical reality in a chromatographic column. In [15], we also did not find a perfect agreement between the numerical data and the Maxwell-expression. However, this disagreement can with the insights gained in part I now be fully understood as a consequence of the fact that we erroneously used the Maxwell-expression for spheres (Eq. (16) in part I), whereas we should have used the cylinder-variant (Eq. (29) in part I) since we were considering cylindrical pillar beds. In [15], the agreement between the CFD data on the one hand and the employed Maxwell- and LD-models on the other hand were about equally good (or bad), so that it was impossible to confidently decide on which one of the two would be most suited to predict the effective diffusion in real packed-bed columns [19].

Hence, given that the deviations between the fitting curves and the simulation data observed in [15] were due to the use of inappropriate models and that much better expressions are available, the present study has been set up to validate these improved models. The reviewers of [15] also had serious concerns about the relevance of the study presented there for 3D systems. The present study therefore also essentially focused on the band broadening in 3D sphere packings. Since our numerical resources are inadequate to simulate random 3D packings, only ordered 3D packings were considered. As will be evidenced further on, this however does not take away from the general validity of the conclusions that can be drawn from the present study. To support this, the effect of randomness was investigated by performing a set of 2D simulations.

At this point, it is also important to realize that a sound and stringent validation of any B-term expression cannot be obtained from experimental work on real columns, because the value of the diffusion coefficient inside the meso-porous zone of the particles is *a priori* unknown under practically relevant chromatographic conditions. This is mainly due to the fact that the observed intra-particle diffusion is to a large extent determined by the so-called stationary phase diffusion [20,21], i.e., the diffusion experienced by the analytes when being in the retained state. Unfortunately, little or no reliable expressions or data are available to predict the value of the stationary phase diffusion coefficient D_s. One of the complications in this respect is that D_s, in many literature reports [20,21], appears to vary quite strongly with the phase retention factor, whereas it has become now become clear that part of this strong relationship might be due to the fact that the reported D_s-values have been measured using the traditional residence time weighted model (RTW-model), which is known from part I and [15] to induce a false additional curvature into the relation between D_s and the retention equilibrium constant [15].

As a consequence, a reliable experimental validation of effective diffusion models is currently only possible in the absence of a phase equilibrium, i.e., under conditions where surface diffusion effects can be excluded. In this case, and provided the geometry of the pore space can be represented as a packing of nano-spheres, the intra-particle obstruction factor can relatively well be predicted by applying the EMT-expressions to the intra-particle level (see also Section 2.5 of part I). This approach has been used by Denoyel et al. [22], who demonstrated that the Maxwell-expression can indeed be confidently used to estimate the diffusion in the meso-pore space as well as in the interstitial void. It also explains why the Maxwell-expression is since long being used in the field of chemical engineering to model pure diffusion effects (i.e., in the absence of a retention equilibrium or surface diffusion) in packed bed columns [23].

For systems with retention, and when surface diffusion plays a significant role, the analytical expressions established in part I can

only be validated using numerical methods, solving the diffusion equations in systems where all local diffusion coefficient values are exactly known.

Also the surprisingly simple EMT-expression for coated-spheres, or, equivalently, porous-shell systems established by Hashin and Shtrikman requires some form of validation, as it is the first time this expression has been used in the field of chromatography. According to the Hashin–Shtrikman solution, the individual porous-shell particles can, despite the presence of a large solid core, still be represented as a uniform zone with a uniform intra-particle diffusion coefficient D_{part}. Even more, this externally observed intra-particle diffusion coefficient can be directly linked to the local diffusion coefficient in the shell layer (where locally $D = D_{pz}$) via a very simple, yet mathematically exact expression for the intra-particle obstruction factor γ_{part}:

$$\gamma_{part} = \frac{D_{part}}{D_{pz}} = \frac{2}{2+\rho^3} \quad \text{(spherical particle case)} \tag{3a}$$

$$\gamma_{part} = \frac{D_{part}}{D_{pz}} = \frac{1}{1+\rho^2} \quad \text{(cylindrical pillar case)} \tag{3b}$$

wherein ρ is the relative core diameter ρ ($\rho = d_{core}/d_{part}$) [3]. This implies that the intra-particle diffusion rate that would be measured by an external observer will be reduced with a given fraction γ_{part} given by Eqs. (3a) and (3b) when a solid core is put in the center of an otherwise unchanged particle (and while keeping the same mobile phase composition because otherwise D_{pz} will vary). The value of this obstruction factor only depends on the relative core diameter ρ, and is independent of the packing arrangement and the value of the retention and diffusion coefficients.

To numerically verify the EMT-expressions presented and discussed in part I, the following numerical verification strategy was adopted. Using CFD simulations, we first calculated the B-term band broadening (via D_{eff}) in ordered packings of uniform spheres (either fully non-porous or fully porous) arranged in either of the three types of ordered sphere packings (simple cubic (sc), body centered cubic (bcc) and face centered cubic (fcc) packings of spheres, see Fig. 2 of part I). Initially, only two different values for the external porosity (resp. $\varepsilon_e = 0.35$ and 0.40) were considered. These values encompass the typical range of porosities encountered in randomly packed beds of uniform spheres. A straightforward critic that could be formulated is that the spheres in an ordered fcc- or bcc-arrangement with $\varepsilon_e = 0.35$ and 0.40 do not touch each other. However, from the observation made in Figs. 5 and 6 of part I, showing that the B-term constant values produced by the Torquato-based model for random packings with $\varepsilon_e = 0.40$ (touching spheres) lies very close to those predicted by the ordered fcc- and bcc-model for the same $\varepsilon_e = 0.40$-porosity (and thus relating to a system with non-touching spheres), it can be inferred that the actual touching of the spheres does not lead to a sudden change in diffusion behavior. To investigate the effect of the touching of the spheres, we also considered an ordered fcc-packing around its closest-packing limit, allowing even for a small overlap of the spheres ($\varepsilon_e = 0.244$). The effect of packing randomness has been investigated as well. For this purpose, we switched to 2D cylinder packings because the diffusion in 2D systems can be computed in a much shorter time than in a 3D system. This was needed because switching from an ordered to a disordered system also automatically implies that much larger geometries, containing much more particles, need to be considered.

The different considered particle packings were subsequently modified by introducing an impermeable sphere (or cylinder) in the center of each spherical particle (Fig. 1a) or cylindrical pillar (Fig. 1b). For each packing type, two or three different core sizes have been considered.

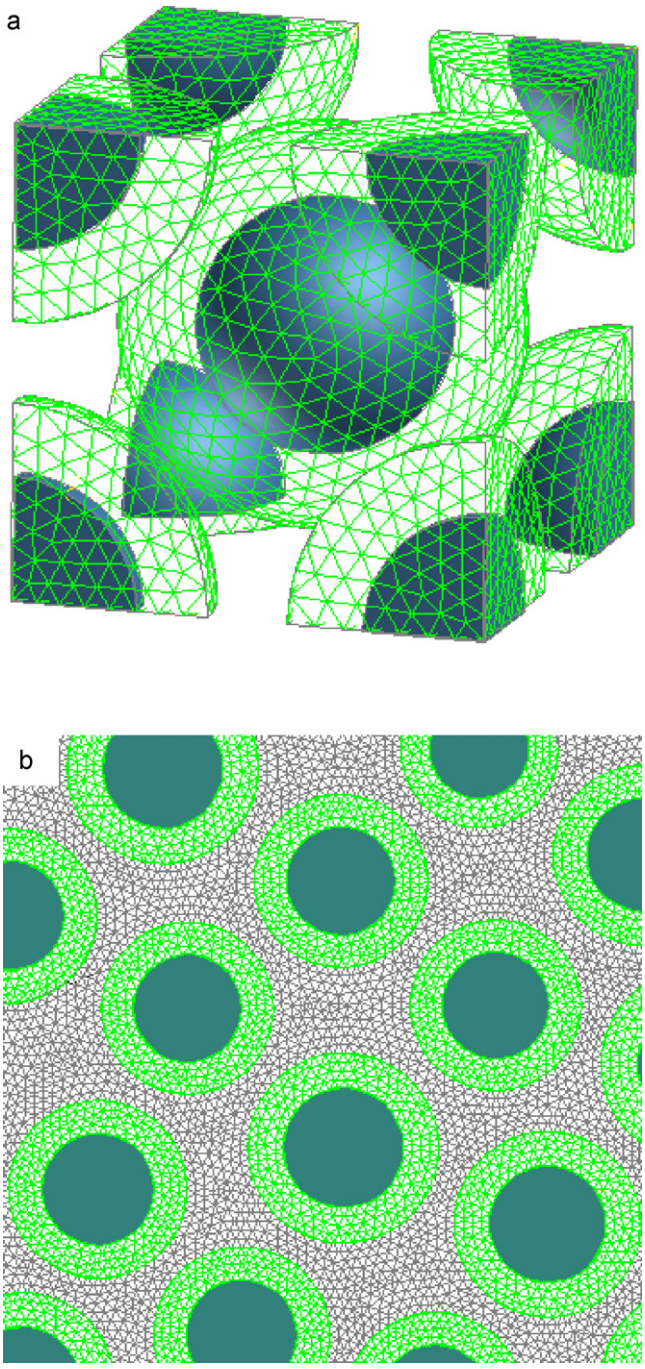

Fig. 1. (a) Unit cell for a body centered cubic packing of particles containing a core with relative radius $\rho = 0.63$. (b) Part of the computational domain used in the 2D simulations.

Next, the obtained results were compared to the most useful EMT-models originating from the study presented in part I. The RTW-model, traditionally used in literature to model the B-term constant and to determine the value of the surface diffusion coefficient [5,7,24], was discarded because this model is physically invalid and leads to erroneous values for D_{part}, as was shown in part I. The LD-model was no longer considered either, because of the uncertainty of the z-value that needs to be used, as well as because of its poor modelling accuracy observed in part I. The latter is the consequence of the fact that the LD-model is based on the physically unsound phase-symmetry assumption (see part I).

2. Geometries and employed numerical procedures

For all different considered packing geometries (fcc, bcc, sc, square and equilateral triangular), except the random packing, the simulation domains were build using a unit cell that was translated several times in the x-direction. Fig. 1a shows an example of one of the considered unit cells, including the employed computational grid and the solid core needed to mimic the porous-shell case. An overview of all considered unit cells for the 3D packings is shown in Fig. 2 of part I. In the x-direction (the diffusion direction), the computational domains were 10–20 particle diameters long. This is the minimum length needed to prevent the tracer from leaving the domain (by diffusion) before the effective diffusion coefficient reaches its steady value. In the other directions the computational domain was sized a single unit cell and symmetry boundary conditions were applied:

$$\frac{\partial c}{\partial n} = 0 \tag{4}$$

For a random packing, it is impossible to identify a unit cell and the size of the computational domain cannot be reduced by using symmetry boundary conditions. As a consequence, much larger simulation domains are needed so that we had to restrict ourselves to 2D cases. The considered random packings were created using a drop-and-roll 2D packing algorithm to pack cylinders with a uniform size distribution with a width of 20%. After the packing procedure, the cylinders were shrunk to obtain the desired bed porosity ($\varepsilon_e = 40\%$). The size of the computational domain was 16 particle diameters wide and 27 particle diameters long. Fig. 1b shows part of the domain. The computational domain for the random packings was slightly longer than the structured ones, because it takes longer before the effective diffusion coefficient reaches a steady-state value in the random case. If the length of the domain would have been shorter, some of the tracer would already have reached the boundaries (in the x-direction) of the domain before the effective diffusion coefficient would have reached its steady-state value. In all cases, the particles had a diameter of 2.7 μm.

All domains (structured and random) were drawn and discretized using a commercial software package (Gambit®). This discretization was done using a tri-mesh meshing scheme. The size of the grid cells was chosen in such a way that the calculated effective diffusion coefficients were grid independent (increasing the grid size caused the effective diffusion coefficient to increase less than 0.1–0.2%). In practice, this came down to dividing each particle in about 1000 (for the circular cross-section of the cylindrical pillars) to 40,000 (for 3D spheres) grid cells (the grid cells outside the particles were of a similar size).

After this discretization step, a commercial computational fluid dynamics software package (Fluent® v. 6.3) was used to solve the diffusion mass balances:

$$\frac{\partial c}{\partial t} = D_m \nabla^2 c \text{ in the mobile zone,}$$

$$\frac{\partial c}{\partial t} = D_{pz} \nabla^2 c \text{ in the porous zone} \tag{5}$$

The boundary condition at the interface between the mobile zone and porous zone, was the following:

$$D_m \left.\frac{\partial c}{\partial n}\right|_{\text{mobile zone}} = \frac{D_{pz}}{K_{pz}} \left.\frac{\partial c}{\partial n}\right|_{\text{porous zone}} \tag{6}$$

For the structured packings, symmetry boundary conditions were imposed at the domain boundaries in the y- and z-directions.

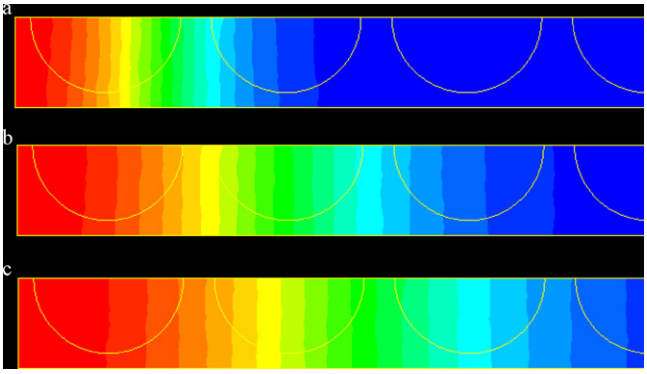

Fig. 2. Visualization of the diffusion process, showing a top view of a body centered cubic packing and the evolution of the tracer species concentration at three different parking times: (a) 4.2 ms, (b) 13.2 ms, and (c) 24 ms. Each different colour represents a 5% fraction of the concentration at the top of the concentration distribution (situated at the left of the represented flow domain, i.e., at the x-symmetry boundary). (For interpretation of the references to color in this figure legend, the reader is referred to the web version of this article.)

At the boundaries in the x-direction, an outlet boundary condition was imposed on one side and a symmetry boundary condition on the other side. In the case of the 2D random packing, there is no symmetry in the x-direction, hence two outlet boundary conditions were imposed. In the y-direction periodic boundary conditions, mimicking an infinitely wide domain, were imposed. The mobile zone was given the properties of water and the meso-porous zone (either the full particle or only the porous-shell layer) was attributed an internal porosity of 0.35. To mimic the start of the peak parking experiments, a thin region (width = 0.2 μm, 7% of a particle) of the flow domain was filled with a tracer liquid having the same physicochemical properties as the rest of the mobile phase. This region was defined at the x-symmetry boundary (or in the middle of the domain in the random packing cases), and extended along the entire domain in the y-direction (and also in the z-direction for 3D cases). In the interstitial space, the tracer was attributed a diffusion coefficient D_m (which was always kept at $D_m = 10^{-9}$ m^2/s), whereas the tracer dye was assigned a diffusion coefficient D_{pz} in the meso-porous zone in the particles. In this meso-porous zone, the tracer species were also subjected to a species equilibrium by introducing a reversible chemical reaction that transforms the freely diffusing species A into a retained species A* via a forward and backward reaction rate combining into a given equilibrium constant $K_{A,pz}$ [13].

A fixed time stepping method was chosen to subsequently solve the diffusion equation using an implicit, segregated solution scheme with a second order implicit unsteady formulation. Typical time step sizes were in the order of 1 ms. At every time step, the 0th, 1st and 2nd order spatial moment of the tracer concentration were reported [13] and the effective diffusion coefficient was calculated using Eq. (1) and the increment in spatial variance that could be derived from the spatial moments.

3. Results and discussion

3.1. Details and accuracy of the simulation

Fig. 2 shows how the iso-concentration planes (expressed as a given fraction of the maximum of the concentration curve) evolve with the time in a top-view of one of the considered sphere packings. The fact that the iso-concentration planes are not perfectly flat but have a rather wavy shape is a consequence of the fact that the geometry of the bed slightly changes with its depth, so that molecules at different depths experience a slightly different diffu-

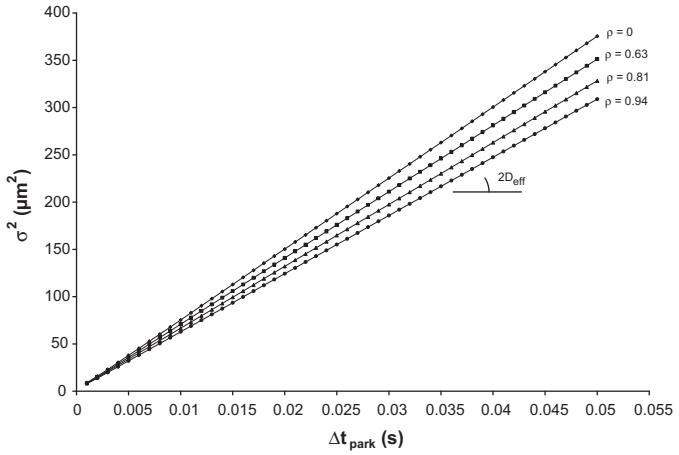

Fig. 3. Variation of the band variance σ^2 with Δt_{park} for $k'' = 5$ and the case of an fcc-packing with $\varepsilon_e = 0.4$, $D_{pz}/D_m = 0.25$ and for different values of ρ ($\rho = 0$, 0.63, 0.81 and 0.94).

sion rate. This in turn induces concentration gradients in the depth of the considered packing, but these effects are well-accounted for in the higher order accuracy EMT-models, as well as in the 3D CFD-simulations.

Fig. 3 shows how $\Delta\sigma^2{}_{diff}$ varies with the considered peak parking times. In agreement with Eq. (1), a perfectly linear relationship is obtained for all considered cases. The 95% confidence intervals on the slopes were smaller than 0.05%. Comparing the computed diffusion rate in a fully open system (no spheres), where the slope of the curves should hence simply be equal to $2.D_m$, we could estimate that the numerical diffusion (originating from the fact that the considered grid cells still have a finite size) was of the order of some 0.15–0.25%.

3.2. Effect of geometry and retention and diffusion coefficients on $\gamma_{eff} = D_{eff}/D_m$ and agreement with the EMT-models

Fig. 4 shows the variation of D_{eff}/D_m with varying retention for the Maxwell and the Cheng–Torquato models. Two other values for D_{pz} have been considered as well (see Fig. S-2 of the SM of part I for the corresponding figures).

Before continuing, it should be kept in mind that, although the results are presented here in terms of γ_{eff}, representing the obstruction factor for the effective longitudinal diffusion, the presented data can also be readily transformed in terms of the B-term constant appearing in any reduced plate height expression using (see Eq. (2)):

$$B = 2\gamma_{eff}(1 + k') \tag{7}$$

It should also be noted that the model curves shown in Fig. 4 are not obtained via curve fitting, but are calculated from scratch (i.e., only using the known values of the retention factor, D_{pz}, ε_e and D_m) using either the Maxwell-based (1st order approximation, red curves) and the Cheng–Torquato based (maximal accuracy solution, black curves) expressions for spherical particles established in part I, respectively given by:

$$\gamma_{eff} = \frac{1}{\varepsilon_T.(1 + k')} \cdot \frac{1 + 2.\beta_1(1 - \varepsilon_e)}{1 - \beta_1(1 - \varepsilon_e)} \quad \text{(Maxwell – based model)} \tag{8}$$

and

$$\gamma_{eff} = \frac{1}{\varepsilon_T.(1 + k')} \left(1 - \frac{3.(1 - \varepsilon_e)}{\Lambda}\right) \quad \text{(Cheng–Torquato based)} \tag{9a}$$

wherein Λ is a parameter that needs to be calculated using:

$$\Lambda = -\beta_1^{-1} + (1 - \varepsilon_e) + b_1\beta_3(1 - \varepsilon_e)^{10/3} + b_2\beta_5(1 - \varepsilon_e)^{14/3} + b_3\beta_3^2(1 - \varepsilon_e)^{17/3} + b_4\beta_7(1 - \varepsilon_e)^6 + b_5\beta_3\beta_5(1 - \varepsilon_e)^7 + b_6\beta_9(1 - \varepsilon_e)^{22/3} \tag{9b}$$

The numerical coefficients for the b_i-coefficients appearing in Eq. (9b) are given in Table 1 of part I. The β_i-parameters appearing in Eqs. (8), (9a) and (9b) are given by (with $i = 1,3,5,\ldots$) [16]:

$$\beta_i = \frac{\alpha_{part} - 1}{\alpha_{part} + (i + 1)/i} \tag{10}$$

This β_1-factor in turn depends on the value of the so-called relative particle permeability α_{part}, which can be readily calculated from the known value of either the phase or zone retention factor (k' or k'') and the value of intra-particle diffusion coefficient D_{part} using:

$$\alpha_{part} = \frac{\varepsilon_e.k''}{1 - \varepsilon_e} \cdot \frac{D_{part}}{D_m} = \frac{(1 + k').\varepsilon_T - \varepsilon_e}{1 - \varepsilon_e} \cdot \frac{D_{part}}{D_m} \tag{11}$$

with k' the phase retention factor (determined with respect to the t_0-marker) and k'' the zone retention factor, related to the former via (see SM of part I):

$$k'' = (1 + k').\frac{\varepsilon_T}{\varepsilon_e} - 1 \tag{12}$$

In the general case, D_{part} is determined by the intrinsic diffusion coefficient (D_{pz}) prevailing in the meso-porous part of the particle and the relative core diameter ρ via the mathematically exact expressions given in Eqs. (3a) and (3b).

In the present study, both D_{pz} and k' are imposed numerically, and also the values of ρ, ε_e and ε_T were known exactly, so that the application of these values into the combination of Eqs. (8)–(11) directly yielded the model curves for γ_{eff} shown in Fig. 4. The excellent agreement between the thus obtained model curves and the numerical data hence provides an excellent mutual validation of both the computational method and the analytical expressions. The data are even refined enough to note (see inset of Fig. 4) the difference between the Maxwell-based model (1st order approximation) and the Torquato-based model for cases with very low permeability (i.e., for $k'' \to 0$). The higher order accurate Torquato-based model clearly goes through the computed data whereas the Maxwell-model (lower order accuracy) slightly overestimates the true value, which is in full agreement with the findings in Figs. 4 and 5 of part I. As regards $k'' = 0$, similar data have been reported by Kim and Chen [25]. The values obtained in that study are in qualitative agreement with the mathematically correct result of Cheng and Torquato, but are slightly off the theoretical prediction. Over the largest part of the curves, the Maxwell- and the Torquato-based model however nearly perfectly coincide.

As can be noted by considering the curves for the different solid core size cases (varying from $\rho = 0$ to 0.94), the EMT-models are also capable of perfectly predicting the effect of the presence of a solid core. To generate the numerical data, the diffusion in the shell-layer (D_{pz}) was kept constant. In agreement with the Hashin–Shtrikman theory, the model curves were produced using the same EMT-expressions as used for the fully porous particles, but now with D_{part} calculated via Eq. (3a) and the known value of D_{pz}. In agreement with the physical expectations, it can clearly be observed that, the larger the core, the more the effective diffusion through the particle and the bed are reduced (obstructed). From the fact that the curves for the different ρ-cases lie more closer together in the low D_{pz}-case (Fig. 4a) than in the high D_{pz}-case (Fig. 4b), it can also be concluded that the obstructing effect of the solid core is more pronounced when the diffusion rate in the meso-porous zone is large

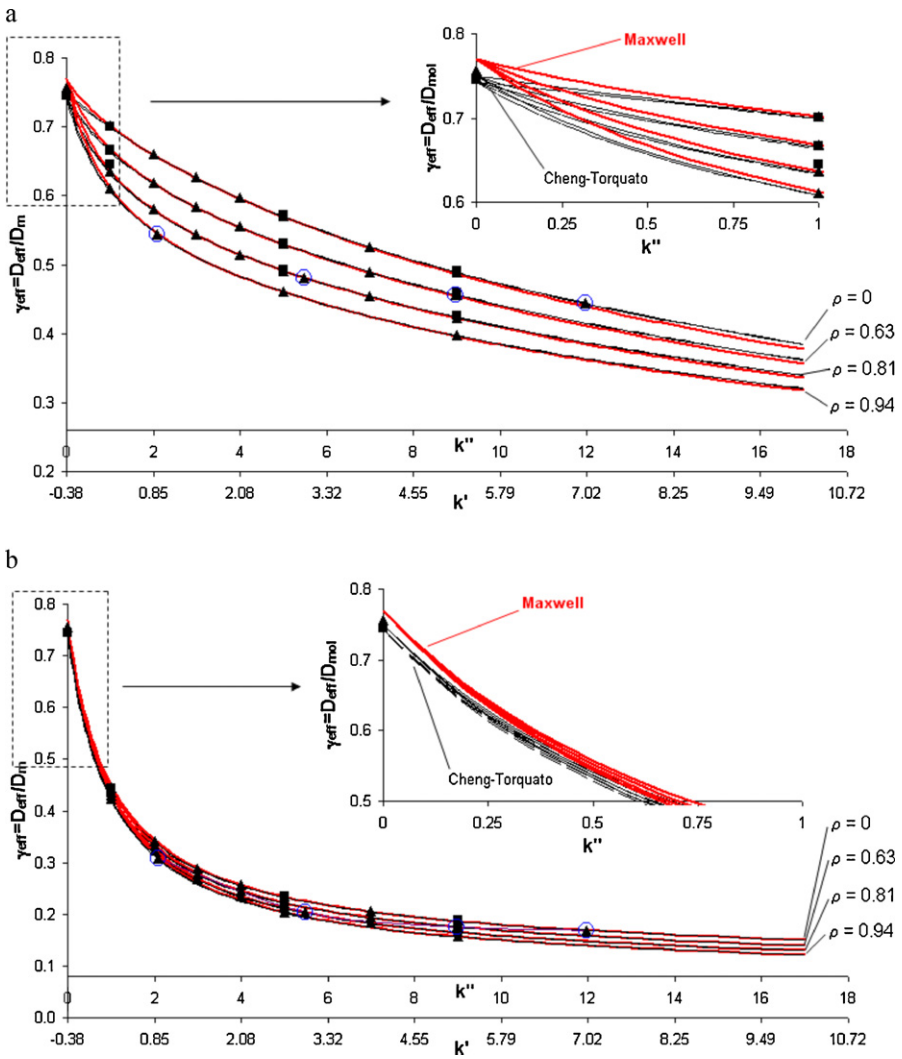

Fig. 4. Variation of D_{eff}/D_m with k' and k'' for ordered sphere packings with various ρ ($\rho = 0$, 0.63, 0.81 and 0.94) and with $\varepsilon_e = 0.4$, for two D_{pz}-cases: (a) $D_{pz}/D_m = 0.5$ and (b) $D_{pz}/D_m = 0.1$). Computational data for a bcc- (■) and an fcc-packing (▲) is shown as well as the Maxwell-model (▬) and the Cheng–Torquato model bcc (– –), fcc (—). The meaning of the blue circled data points is given in the text. (For interpretation of the references to color in this figure legend, the reader is referred to the web version of this article.)

and is less pronounced when this rate is already small. This is also in agreement with one's physical intuition, because the dominant diffusion trajectory followed by the analytes in the latter case is anyhow already situated in the interstitial void space where the diffusion is 10 times faster. As a consequence, the reduction of the intra-particle diffusion induced by the solid core only has a limited effect. The effect of the presence of a solid core is further discussed in Section 3.3.

Comparing the agreement between the model curves and the computed data with that obtained for the Maxwell-model in [15], it can be concluded that the computed D_{eff}-data now fit much better with the Maxwell-model than was the case in [15]. In hindsight, we can now attribute this to the fact that in [15] the sphere-variant of the Maxwell-model was used to model a cylinder packing, whereas obviously the cylinder variant should have been used. The case of a cylinder packing is reconsidered in Fig. 5, showing the variation of D_{eff}/D_m with varying retention in two types of cylinder packings (equilateral triangular and cubic arrangement) and for different cylindrical core sizes (ranging from $\rho = 0$, fully porous, up to $\rho = 0.81$).

The red and black curves in Fig. 5 respectively represent the cylinder variant of the Maxwell-model and the three-point Torquato-model for cylinders, respectively given by (see Section 2.4 of part I):

$$\gamma_{eff} = \frac{1}{\varepsilon_T.(1+k')} \cdot \frac{1+\beta_1(1-\varepsilon_e)}{1-\beta_1(1-\varepsilon_e)} \quad \text{(Maxwell – based model)} \tag{13}$$

and

$$\gamma_{eff} = \frac{1}{\varepsilon_T.(1+k')} \cdot \frac{1+\beta_1(1-\varepsilon_e)-\varepsilon_e\zeta_2{\beta_1}^2}{1-\beta_1(1-\varepsilon_e)-\varepsilon_e\zeta_2{\beta_1}^2}$$

(Torquato-based model) (14)

The parameter ζ_2 appearing in Eq. (14) is the so-called three-point parameter which needs to be calculated using an expression of the form:

$$\zeta_2 = a_1(1-\varepsilon_e)\exp(a_2(1-\varepsilon_e)) \tag{15}$$

using the a_i-coefficients given in Table 1b of part I.

The observations that could be made from Fig. 4 clearly also hold for the cylinder packing case shown in Fig. 5: excellent fit of the data with the Maxwell- and Torquato-based models (with the latter to be preferred in the small k''-range where the geometry of the packing starts to play a dominant role) and a stronger reduction

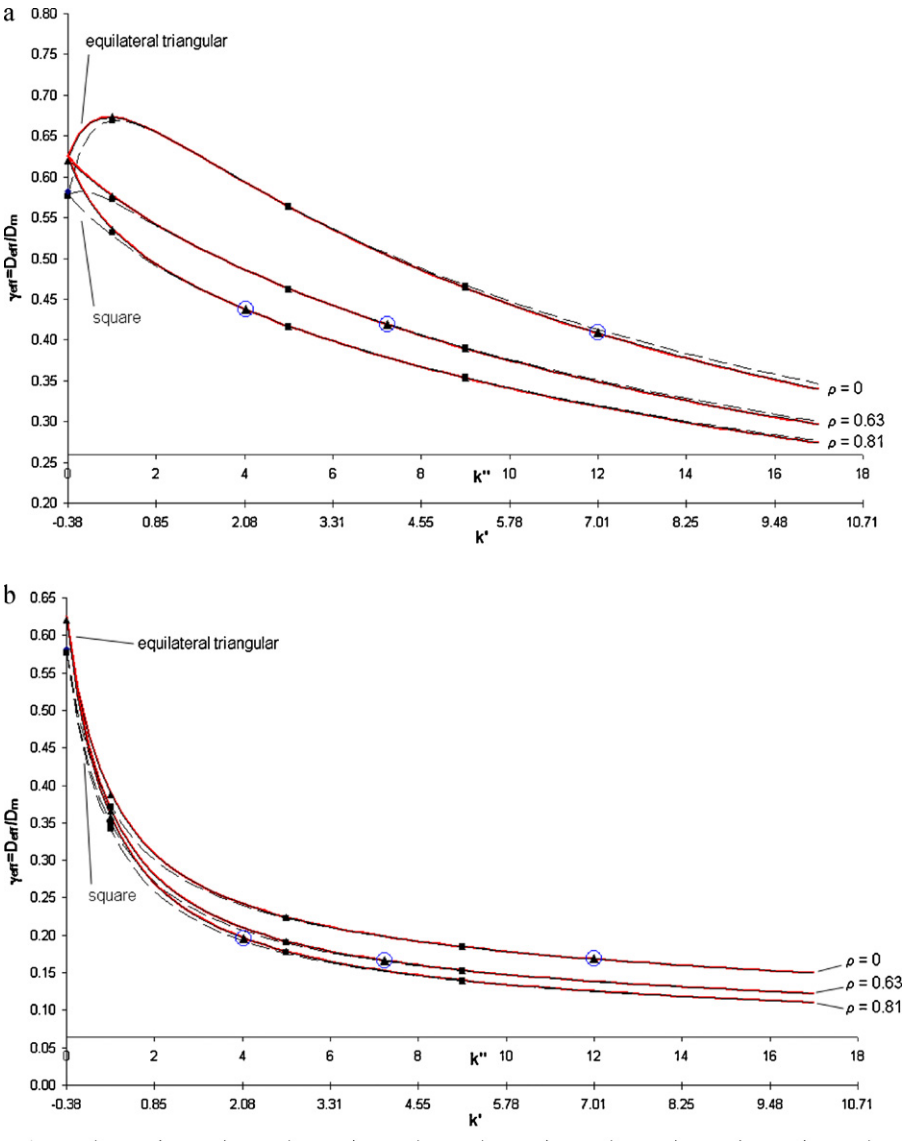

Fig. 5. Variation of D_{eff}/D_m with k' and k'' for ordered cylinder packings with various ρ ($\rho = 0$, 0.63 and 0.81) and with $\varepsilon_e = 0.4$, for two D_{pz}-cases: (a) $D_{pz}/D_m = 0.5$ and (b) $D_{pz}/D_m = 0.1$. Computational data for a square array (■) and an equilateral triangular array (▲) of cylinders is shown as well as the Maxwell-model (▬) and the Torquato model with $\zeta_2 = 9.70 \times 10^{-2}$ for the square array (– –), $\zeta_2 = 8.07 \times 10^{-3}$ for the equilateral triangular array (—). The meaning of the blue circled data points is given in the text. (For interpretation of the references to color in this figure legend, the reader is referred to the web version of this article.)

induced by the solid core in the large D_{pz}-case as compared to the low D_{pz}-case. The parallelism between Figs. 4 and 5 also shows that a 2D representation produces a good qualitative insight in the diffusion behavior of 3D systems. This could in fact already be inferred from part I, where it could be noted that the EMT-expressions for cylinders and spheres are very similar and only differ by the value of the numerical constant appearing in it.

In the present study, the qualitative analogy between 2D and 3D systems has been used to assess the effect of the packing randomness on the diffusion behavior of chromatographic packings. From part I, we already know that there is a broad range of retention factors wherein the exact packing geometry anyhow only has little or no effect on the observed effective longitudinal diffusion, so that the difference between ordered and random packings should anyhow be very small (and even non-existent when α_{part} is close to unity). This is now confirmed in Fig. 6, showing the computed data points for the random packing geometry shown in Fig. 1b. Noting that the Maxwell-model curve in Fig. 6 follows exactly the same trajectory as in Fig. 5 (the Maxwell-model neglects any close-neighbour interactions and yet hence produces the same D_{eff}-estimate for an ordered and a random packing), the impact of randomness on the longitudinal diffusion can be readily assessed by comparing the position of the computed data points with respect to the Maxwell-model curve (red curve). As can be noted, the data points for $k' = 5$ and 2.5 nearly perfectly coincide with the Maxwell-curve, showing that the effect of randomness is negligible. For larger k', the high order accuracy Torquato-based curves (plain black curve for the equilateral triangular array and dashed black curve for the square array) and the Maxwell-curve anyhow lie very close to each other, so that in this range also only a small effect of randomness can be expected. For very small k', the computed (random case) data points lie slightly below the perfectly ordered equilateral triangular case shown in Fig. 5 (1% for $k' = 0.2$), while the agreement with the theoretical prediction remains good. For the non-porous pillar case ($k'' = 0$), the difference between the random and the ordered equilateral triangular case is 6%. The $k'' = 0$-data point also lies relatively far away the model curve. We assume this can be explained by the fact that the theoretical value of ζ_2 predicted via Eq. (15), using a_i-parameter values based on the calculations in [26], most probably still depends on the actual degree of randomness and packing type.

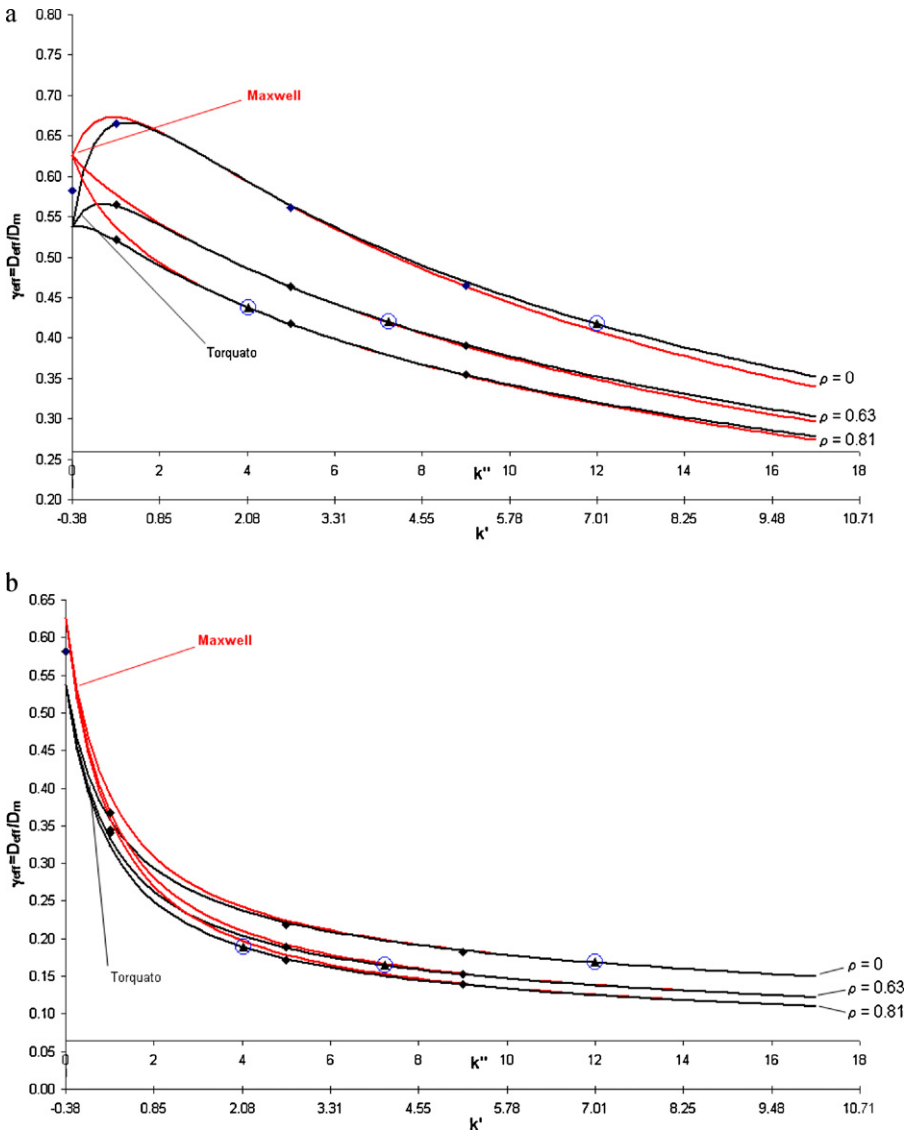

Fig. 6. Variation of D_{eff}/D_m with k' and k'' for a random cylinder packings with various ρ ($\rho = 0$, 0.63 and 0.81) and with $\varepsilon_e = 0.4$, for two D_{pz}-cases: (a) $D_{pz}/D_m = 0.5$ and (b) $D_{pz}/D_m = 0.1$) Computational data (▲) are shown as well as the Maxwell- (▬) and the Torquato-model (—) with $\zeta_2 = 1.79 \times 10^{-1}$. The meaning of the blue circled data points is given in the text. (For interpretation of the references to color in this figure legend, the reader is referred to the web version of this article.)

Eq. (15) produced a value of $\zeta_2 = 0.18$, and this is also the value used to establish the black model curves in Fig. 6. On the other hand, we found that the Torquato-based model curve can be perfectly fitted to the computed data point when taking $\zeta_2 = 0.09$. As a conclusion, it is assumed that for the case of random packings, the value of ζ_2 produced by Eq. (15) is only indicative and might still vary strongly depending on the exact structure of the bed.

To investigate whether any special diffusion effect is induced if going from a situation wherein the particles are "hanging" in space (as is assumed in the data shown in Figs. 4–6) versus the case wherein they actually touch, we also simulated the effective diffusion in a 3D fcc-packing with $\varepsilon_e = 0.244$, i.e., for the case wherein the spheres actually touch. As can be noted from Fig. 7, the general conclusions that could already be drawn from Figs. 4 and 5 still apply (Maxwell fits very well over broad range of k'-values for any D_{pz}-values, while a near-perfect agreement is obtained using the Torquato-model; effect of core can be exactly represented using Eqs. (3a) and (3b)).

This suggests that the general rules that can be drawn from the present study hold irrespective of the fact whether the included particle or pillar regions actually touch or not. The fact that no special diffusion effect is induced when a sphere suspension reaches its close-packing limit could also already be inferred from Fig. 3 of part I, where the represented D_{eff}/D_m-values vary very smoothly with the external porosity ε_e and display no strong sudden change in the vicinity of the close-packing limit (denoted by fx1). In Fig. 8 of the present part, this is reconfirmed for the case of fully porous particles. Grouping all considered ε_e-values, Fig. 8 in fact complements Fig. 4 which only represent one packing density ($\varepsilon_e = 0.40$). Plotting D_{eff}/D_m versus ε_e, Fig. 8 now not only reconfirms that the computed data agree very well with the EMT-model, but it also shows that the close-packing limit is approached without noting any sudden change in effective diffusion rate. Whereas Fig. 8 only shows the data relating to the fully porous particle case, it should be noted that fully similar graphs were obtained for the different considered porous-shell cases (data not shown), as well as for all different considered cylinder packing cases (data also not shown). Fig. 8 also reconfirms another finding that was already apparent in Figs. 4–7, i.e., that the effect of the packing geometry is largest (albeit still very small) when k'' turns to zero (fully solid particle

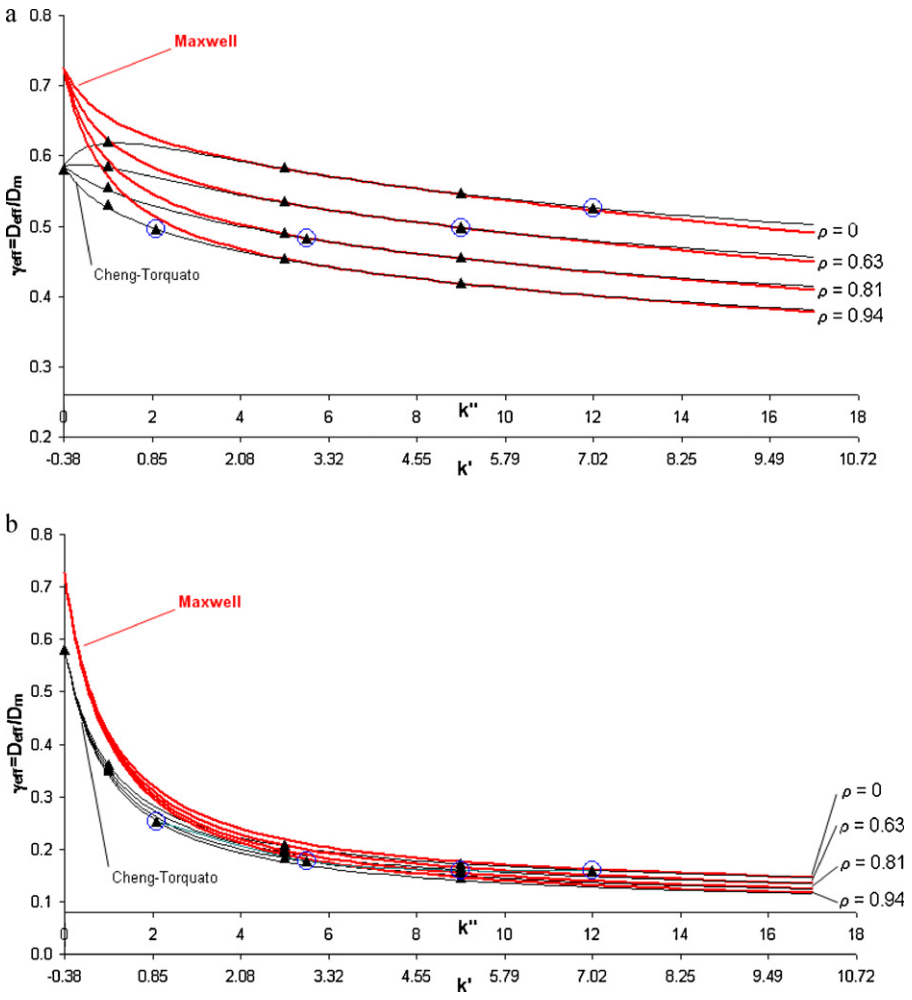

Fig. 7. Variation of D_{eff}/D_m with k' and k'' for an fcc-packing of touching spheres with various ρ (ρ = 0, 0.63, 0.81 and 0.94) and ε_e = 0.244 (touching spheres with even a slight overlap), for two D_{pz}-cases: (a) D_{pz}/D_m = 0.5 and (b) D_{pz}/D_m = 0.1). Computational data for the fcc-packing (▲) is shown as well as the Maxwell-model (▬) and the Cheng–Torquato model (—). The meaning of the blue circled data points is given in the text. (For interpretation of the references to color in this figure legend, the reader is referred to the web version of this article.)

limit). In Fig. 8, this limit corresponds to the upper bundle of curves, where indeed the curves representing the Maxwell-model and the Cheng–Torquato model diverge in the small ε_e-range.

For all other k''-cases, the curves for the Maxwell-model (based on the dilute suspension approximation) and the Cheng–Torquato model (taking close-neighbour interactions into account) nearly perfectly coincide. This implies that the dominant factor determining the effective longitudinal diffusion in chromatographic columns filled with fully porous or porous-shell particles are the external porosity, the intra-particle diffusion constant and the retention factor, and not the actual microscopic packing arrangement or the fact that the spheres actually touch or not.

3.3. *Effect of the presence of a solid core on D_{part} and γ_{eff}*

The effect of the relative core diameter ρ on the computed curves observed in Figs. 4–7 for a given value of k' or k'' is perfectly in line with the coated-particle model of Hashin–Shtrikman (see Eqs. (3a) and (3b)). This is investigated in Fig. 9. The γ_{part}-data points shown there have been calculated as the reduction of the D_{part}-value that is needed in Eq. (9a), (9b) or (14) to go from the D_{eff}-value numerically computed for the fully porous particle case (ρ = 0) to the D_{eff}-value numerically computed for any of the given considered porous-shell cases. Doing this calculation for all considered cases, it was striking to note that the same γ_{part}-value was obtained for all cases with the same $K_{A,pz}$-value. This is in full agreement with the Hashin–Shtrikman theory expressed by Eqs. (3a) and (3b), showing that D_{part} only depends on ρ, provided of course the D_{pz}-value appearing in the left hand side of (Eqs. (3a) and (3b)) remains constant. In practice, D_{pz} is guaranteed to remain constant when comparing cases with the same meso-porous zone material and with the same mobile phase composition, i.e., with the same intrinsic $K_{A,pz}$. The latter can be noted from Eqs. (44) and (51) of part I, showing that D_{pz} is fully determined by the value of $K_{A,pz}$, which remains unchanged as long as the same mobile phase is being used.

Considering the constant mobile phase-composition case, the effective retention factors k'' and k' will inevitably decrease with increasing ρ, because a growing solid core also implies that less volume is available for retention. It can easily be verified [1] that, regardless of whether one expresses the retention in terms of the zone or phase retention factor, the presence of a solid core will reduce the actual retention factor with a factor $(1-\rho^3)$ when $K_{A,pz}$ is the same (i.e., for the same mobile phase). This can also be directly noted from Eqs. (S-8a) and (S-8b) of the SM of part I, yielding:

$$k' = \frac{(1-\varepsilon_e).(1-\rho^3).(1-\varepsilon_{pz}).K_{A,pz}}{\varepsilon_T} \tag{16}$$

$$k'' = \frac{1-\varepsilon_e}{\varepsilon_e}.(1-\rho^3).[\varepsilon_{pz}+(1-\varepsilon_{pz}).K_{A,pz}] \tag{17}$$

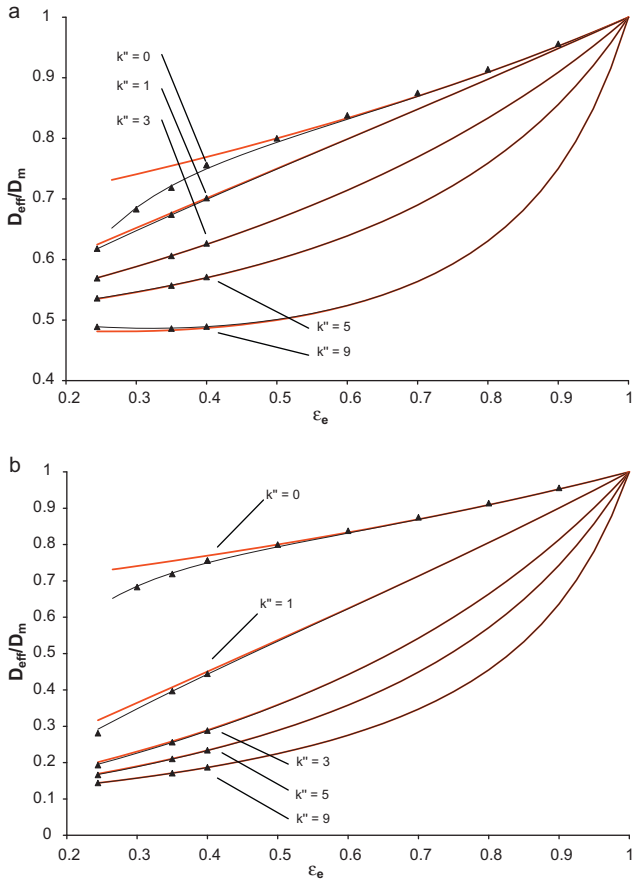

Fig. 8. Plot of D_{eff}/D_m as a function of the packing density ε_e for an fcc-packing of spheres. Five different $K_{A,pz}$-values are considered, resulting in five different k''-values at $\varepsilon_e = 0.4$. The solid data points (▲) refer to the simulation data for $\varepsilon_e = 0.244$, 0.35 and 0.4 already shown in Figs. 4 and 7 and in Fig. S-5 of the SM). The represented model curves have been obtained using the Maxwell-based model ( ) and the Cheng–Torquato based model (—). (a) $D_{pz}/D_m = 0.5$ and (b) $D_{pz}/D_m = 0.1$.

As a consequence, the situation wherein the core size of the particles is gradually changed while keeping the mobile phase composition constant leads to the kind of trajectory indicated by the blue circles added to Figs. 4–7. The evolution of the γ_{part}-values along the trajectory indicated by the blue circles was subsequently represented Fig. 9. As can be noted, these values perfectly agree with the Hashin–Shtrikman curves predicted by Eqs. (3a) and (3b). This clearly holds for all the different geometries (both ordered and disordered) and D_{pz}-values considered in Figs. 4–8, and for the spherical as well as for cylindrical particles.

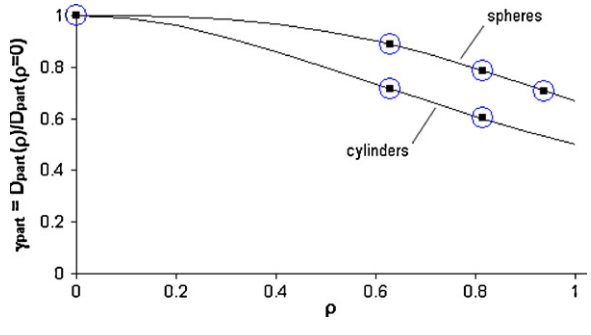

Fig. 9. Variation of the numerically computed γ_{part}-values (see text for details) obtained for the blue circled data points shown in Figs. 4–7 as a function of ρ for spheres and cylinders. The solid lines represent the Hashin–Shtrikman model given by Eqs. (3a) and (3b). (For interpretation of the references to color in this figure legend, the reader is referred to the web version of this article.)

It was also verified that, whatever other k''-value was selected as the starting point on the fully porous particle curve ($\rho = 0$), the corresponding data points of the constant $K_{A,pz}$-trajectory always fell on the same Hashin–Shtrikman curve. This curve is clearly independent of the geometry, as the data points for the different packing types (fcc and bcc for spherical particles and square and equilateral triangular for cylindrical pillars), the different ε_e-cases ($\varepsilon_e = 0.40, 0.35, 0.244$), the different D_{pz}-cases ($D_{pz} = 5 \times 10^{-10}$ m^2/s, 2.5×10^{-10} m^2/s, 1×10^{-10} m^2/s, 5×10^{-11} m^2/s) and the disordered case all fall on the same curve, in agreement with the theory [27,28].

Also interesting to note, and also partly counterintuitive, is that the intra-particle obstruction factor γ_{part} only decreases steadily and reaches a value that is finite (and not zero) when the relative core size approaches unity. This can be understood as follows. Whereas a growing core indeed leads to an ever growing diffusion obstruction, the growing core at the same time also reduces the volume over which the species need to diffuse. The latter partly counters the effect of the growing obstruction, obviously leading to a non-zero obstruction factor when approaching the $\rho = 1 -$ limit.

Whereas the presence of a solid core leads to a clear reduction of the intra-particle diffusion coefficient, the effect of the solid core on the effective longitudinal diffusion in the whole bed (represented by γ_{eff}) is less straightforward. To better understand this, we have investigated the effect of a growing core on γ_{eff} in more detail.

Considering first the case of a constant mobile phase composition, leading to the important simplification that D_{pz} remains invariable, we can say that the presence of a solid core has two effects on γ_{eff}. Firstly, it reduces the intra-particle diffusion rate with a given fraction γ_{part}, directly given by Eqs. (3a) and (3b) for the constant mobile phase-case. Secondly, it also reduces the effective retention factors k'' and k', in agreement with Eqs. (16) and (17).

The effect of a growing core size in the case of a constant mobile phase composition can in fact readily be visualized when following the trajectory indicated by the blue circles in Figs. 4–7 from right to left (i.e., by starting on the fully porous particle curve, $\rho = 0$). The same data points are also represented in Fig. 10, together with the EMT-model lines. Apart from the blue circled data points, also other starting points on the fully porous particle curve have been considered (corresponding to different k''_{FP}-values). Fig. 10a shows that, in cases with a high D_{pz} and under constant mobile phase conditions, the presence of a small solid core leads to a slight decrease of γ_{eff}, because the increased intra-particle obstruction induced by the presence of the solid core is the dominant effect. However, when the core becomes larger and larger, the increase in γ_{eff} that always accompanies a decrease in retention starts to dominate and γ_{eff} increases (all EMT-models namely predict an increase in γ_{eff} when k'' or k' decreases, see for example Figs. 4–7). When D_{pz} is small (Fig. 10b), in which case the variation of γ_{eff} with k' is very strong (as can for example be witnessed from the difference between Fig. 4a and b), the initial reduction of γ_{eff} is not observed, because the reduced-retention effect of the solid core immediately dominates the intra-particle obstruction effect. As can be noted by comparing the curves for the different $k'_{fully\ porous}$-values, the effect on γ_{eff} depends in an intricate way on the k'-value of the fully porous particle reference case.

For the practically more relevant case, i.e., that wherein the mobile phase would be adapted to keep the same retention factor when considering differently sized solid cores, the situation is more difficult to analyze since now both D_m and D_{pz} will change when considering different core sizes (because of the change of D_{pz} with $K_{A,pz}$). However, neglecting these effects, which to a first approximation is always possible, the effect of the presence of a solid core

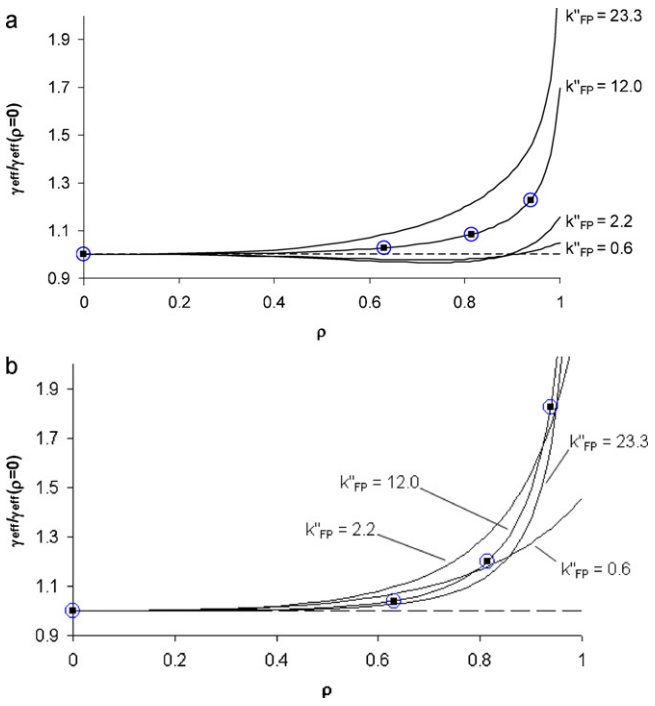

Fig. 10. Variation of γ_{eff} with ρ for different reference retention factors k''_{FP} (with $k''_{FP} = k''$ for case with $\rho = 0$) for an fcc-packing of spheres, and for two D_{pz}-cases: (a) $D_{pz}/D_m = 0.5$ and (b) $D_{pz}/D_m = 0.1$. The blue circled data points relate to the blue circled data points shown in Fig. 4. They follow the k''-trajectory obtained by starting at k''_{FP} for $\rho = 0$ and subsequently assuming that $K_{A,pz}$ remains constant while ρ increases. The solid lines were calculated according to the Cheng–Torquato based model (—). The horizontal dashed line represents the case where $\gamma_{eff} = 1$. (For interpretation of the references to color in this figure legend, the reader is referred to the web version of this article.)

can readily be visualized by noting how the curves for the different ρ-cases presented in Figs. 4–7 decrease for a given constant k''- or k'-value. Doing so, it can be noted that the presence of a solid core always leads to a net reduction of the effective longitudinal diffusion in any possible case. This is fully in line with the simple physical fact that the cores induce an additional obstruction to the effective longitudinal diffusion.

4. Conclusions

Using computational fluid dynamics simulations of the B-term band broadening under retained and non-retained species condition, it can be shown that the exact analytical expressions that can be derived from the effective medium theory (EMT) can exactly represent the effective diffusion or B-term band broadening under liquid phase chromatographic conditions in a wide variety of geometries. On the other hand, the excellent agreement also validates the adopted numerical calculation procedures. The study also shows that 2D and 3D packings produce qualitatively very similar diffusion effects, so that the former can be used to gain insight in the effective diffusion processes occurring in the latter.

Under most conditions, the simple Maxwell-based expression describes the computed data already very well (especially in the $k' > 0.5$-range). This implies that Eq. (8) (or the Torquato-based models if one would go for the ultimate precision) should be used as the new standard for the prediction of the B-term constant, as a replacement of the residence time-weighted B-term expressions that have been used up to now in the field of chromatography. The fact that the Maxwell-model, containing no information about its neighbouring particles, already provides such accurate predictions also implies that, apart from the bulk mobile phase diffusivity D_m, the dominant factors determining the effective longitudinal diffusion in chromatographic columns filled with fully porous or porous-shell particles are the external porosity, the intra-particle diffusion constant and the retention factor, and not the actual microscopic packing arrangement or the fact that the spheres actually touch or not.

In agreement with theory, the EMT-expressions describing the intra-particle obstruction caused by the presence of a solid core, resp. $\gamma_{part} = 2/(2+\rho^3)$ for spherical particles and $\gamma_{part} = 1/(1+\rho^2)$ for cylinders (ρ is the ratio of the core to the particle diameter, $\rho = d_{core}/d_{part}$), hold independently of the geometry of the packing, the value of the diffusion coefficients and the equilibrium constant and the size of the core. This rule also implies that, if considering equal mobile phase conditions, the presence of the solid core will never reduces the particle contribution to the B-term band broadening below 66% (50% in case of cylindrical pillars) compared to a fully porous particles with the same meso-porous zone characteristics.

Comparing the porous-shell and the fully porous particles under equal mobile phase conditions, the presence of a small solid core can lead (when the diffusion coefficient D_{pz} governing the meso-porous zone is large) to a decrease of the effective longitudinal diffusion obstruction factor γ_{eff}, but, when the core exceeds a given critical size, γ_{eff} rapidly increases with the increasing diameter, until eventually the (high) γ_{eff}-value of a non-porous particle column is reached. When D_{pz} is small, γ_{eff} increases monotonously with increasing core diameter. Comparing the porous-shell and the fully porous particles under equal retention factor conditions (which corresponds to comparing the different ρ-curves in Figs. 4–7 along any possible vertical line), the presence of a growing solid core will to a first approximation always lead to a net reduction of the of the effective longitudinal diffusion, thus reflecting the obvious additional obstruction caused by the presence of the impermeable solid cores.

References

[1] A. Cavazzini, F. Gritti, K. Kaczmarski, N. Marchetti, G. Guiochon, Anal. Chem. 79 (2007) 5972.
[2] K. Kaczmarski, G. Guiochon, Anal. Chem. 79 (2007) 4648.
[3] F. Gritti, A. Cavazzini, N. Marchetti, G. Guiochon, J. Chromatogr. A 1157 (2007) 289.
[4] J.H. Knox, L. McLaren, Anal. Chem. 36 (1964) 1477.
[5] J.H. Knox, H.P. Scott, J. Chromatogr. 282 (1983) 297.
[6] J.H. Knox, J. Chromatogr. A 831 (1999) 3.
[7] K. Miyabe, Y. Matsumato, G. Guiochon, Anal. Chem. 79 (2007) 1970.
[8] A. Felinger, A. Cavazzini, M. Remelli, F. Dondi, Anal. Chem. 71 (1999) 4472.
[9] A. Cavazzini, F. Dondi, A. Jaulmes, C. Vidal-Madjar, A. Felinger, Anal. Chem. 74 (2002) 6269.
[10] F. Dondi, A. Cavazzini, L. Pasti, J. Chromatogr. A 1126 (2006) 257.
[11] M.R. Shure, R.S. Maier, D.M. Kroll, H.T. Davis, Anal. Chem. 74 (2002) 6006.
[12] S. Khirevich, A. Hltzel, S. Ehlert, A. Seidel-Morgenstern, U. Tallarek, Anal. Chem. 81 (2009) 4937.
[13] P. Gzil, N. Vervoort, G.V. Baron, G. Desmet, Anal. Chem. 75 (2003) 6244.
[14] J. Billen, P. Gzil, G. Desmet, Anal. Chem. 78 (2006) 6191.
[15] G. Desmet, K. Broeckhoven, J. De Smet, S. Deridder, G.V. Baron, P. Gzil, J. Chromatogr. A 1188 (2008) 171.
[16] S. Torquato, J. Appl. Phys. 58 (1985) 3790.
[17] H. Cheng, S. Torquato, Proc. R. Soc. Lond. A 453 (1997) 1331.
[18] S. Torquato, Random Heterogeneous Materials, Springer Science & Business Media, New York, 2002.
[19] K. Broeckhoven, D. Cabooter, F. Lynen, P. Sandra, G. Desmet, J. Chromatogr. A 1188 (2008) 189.
[20] K. Miyabe, J. Chromatogr. A 1167 (2007) 161.
[21] K. Miyabe, G. Guiochon, J. Chromatogr. A 1217 (2010) 1713.
[22] M. Barrande, R. Bouchet, R. Denoyel, Anal. Chem. 79 (2007) 9115.
[23] E.L. Cussler, Diffusion, Mass Transfer in Fluid Systems, Cambridge University Press, Cambridge, UK, 1984.
[24] R.W. Stout, J.J. Destefano, L.R. Snyder, J. Chromatogr. 282 (1983) 263.
[25] A.S. Kim, H.Q. Chen, J. Membr. Sci. 279 (2006) 129.
[26] S. Torquato, F. Lado, Proc. R. Soc. Lond. A 417 (1988) 59.
[27] Z. Hashin, S. Shtrikman, J. Appl. Phys. 33 (1962) 3125.
[28] Z. Hashin, J. Comp. Mater. 2 (1968) 284.